Highlights:

- Ultra-thin Co, Fe-doped $Ni(OH)_2$ nanosheet arrays were grown onto nickel foam.
- A water electrolyser cell was assembled of asymmetric electrodes of Co/Fe-$Ni(OH)_2$.
- A cell voltage of 1.59 V was achieved at a current density of 10 mA cm^{-2}.

Graphical Abstract

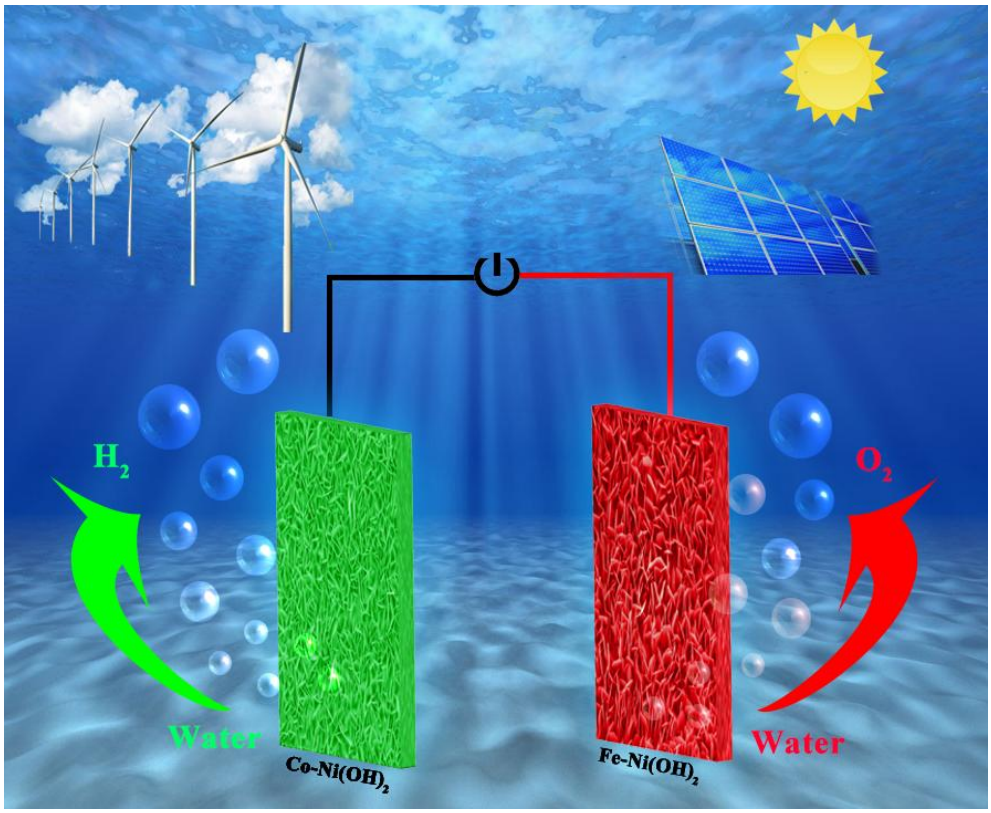

A highly efficient water electrolyser cell assembled by asymmetric array electrodes based on Co, Fe-doped $Ni(OH)_2$ nanosheets

Yutai Wu,[1] Shan Ji[2], Hui Wang,[1] Bruno G. Pollet[3], Xuyun Wang,[1] Rongfang Wang[1**]*

[1] State Key Laboratory Base for Eco-Chemical Engineering, College of Chemical Engineering, Qingdao University of Science and Technology,

Qingdao, 266042, China

[2] College of Biological, Chemical Science and Chemical Engineering, Jiaxing University, Jiaxing, 314001, China

[3] Department of Energy and Process Engineering, Faculty of Engineering, Norwegian University of Science and Technology (NTNU) NO-7491 Trondheim, Norway

Corresponding Author

Shan Ji (*): jishan@zjxu.edu.cn, Tel./fax: +86 (0)15024355548

Rongfang Wang(**): rfwang@qust.edu.cn, Tel./fax: +86(0)17866858722

Abstract

Hydrogen is an “ideal” clean sustainable energy source if it is produced via water electrolyser using power generated by renewable energy systems (RES) such as solar panels and wind turbines. In this study, cobalt (Co) and iron (Fe) doped nickel (Ni) hydroxide nanosheets directly formed onto the surface of Ni foam are synthesized and developed for use as hydrogen evolution reaction (HER) and oxygen evolution reaction (OER) catalysts. When Co-doped nickel hydroxide is used as HER catalyst, it exhibited a high HER activity with a durability better than Pt/C. The *as*-prepared Fe-doped nickel hydroxide show an OER activity, which is even higher than that of RuO_2. When Fe-doped nickel hydroxide and Co-doped nickel hydroxide are both used as HER and OER catalysts in a water electrolyser cell, a current density of 10 mA cm^{-2} at a cell voltage of 1.59 V is observed, a similar value than that obtained for a water electrolyser based on state-of-the-art RuO_2 and Pt/C catalysts. Moreover, the *as*-prepared Fe, Co doped nickel hydroxide also exhibit a good durability when compared to RuO_2 and Pt/C under water electrolyser conditions.

Keywords: Fe-doped nickel hydroxide; Co-doped nickel hydroxide; array electrode; electrocatalyst; water splitting.

1. Introduction

Hydrogen (H_2) is an "ideal" sustainable energy carrier for mobile and stationary power applications, as it can be produced by using power generated by solar panels and wind turbines by simply splitting water.[1-4] Two reactions, namely the hydrogen evolution reaction (HER) and the oxygen evolution reaction (OER), are two important electrochemical processes occurring during water electrolysis.[5-8] Platinum-group-metal (PGM) based materials are usually regarded as efficient catalysts for the HER and OER owing to clearly reduce the large HER and OER overpotentials (η),[9-11] which severely impede the deployment of large-scale water electrolysers due to the high-cost and scarcity of PGM catalyst. Recently, earth-abundant and low-cost transitional metal based (TMB) catalysts, such as transitional metal hydroxides and oxides,[12-14] have attracted much research attention and have been intensively explored due to their high electrocatalytic performance and long-term stability.[15-17] Among these TMB catalysts, $Ni(OH)_2$ is one of the most promising HER and OER electrocatalysts due to its low-cost and high electrocatalytic activity.[5, 18, 19] Evidence showed that the edge of $Ni(OH)_2$ promotes water dissociation and the production of hydrogen intermediates[20, 21], Although fast advances have been made in the development of $Ni(OH)_2$ catalysts for HER and OER. However, the traditional method of synthesizing $Ni(OH)_2$ under alkaline conditions actually results in the thickening of the nanosheets due to the rapid and non-subjective hydrolysis of nickel salts, which inevitably leads to a reduction in the contact area between the catalyst and the electrolyte, [22] their electrocatalytic activity and durability still cannot match PGM

catalysts.

Recent development has shown that designing and tuning the nanostructure and chemical composition of the catalysts can efficiently enhance the HER and OER activity. For example, it was shown that electrodes made of hydrotalcite-like $Ni(OH)_2$ nanosheets directly grown on Ni foam support through hydrothermal process, could deliver an overpotential of 172 mV at a current density of 20 mA cm^{-2} towards the HER and an overpotential of 330 mV at 50 mA cm^{-2} towards the OER in 1.0 M KOH electrolyte.[5] $Ni(OH)_2$ nanosheets grown onto Ni_3S_2 reported by Zhao *et al.* could achieve high OER activity with a low overpotential of 270 mV at a current density of 20 mA cm^{-2} towards the OER.[23] It was also reported that doping different ions, such as Fe, Co into the Co or Ni oxides and hydroxides can efficiently improve the electrocatalytic activity via tuning the electronic structure.[12, 24, 25] In this case, Fe doped Ni hydroxide films delivered higher electrocatalytic activities towards the OER than those found with Ni hydroxide, and the obtained catalytic activity could be tuned by adjusting the amount of doped Fe.[26] It was found that the Fe-O bond with short length yielded improved adsorption energy of intermediates formed during the electrocatalytic reaction, in turn resulting in low overpotential values towards the OER.[27] Apart from Fe ion, it was also found that Co could be used as a doping agent for nickel-based compound in order to improve catalytic properties. Recently, developed Co-doped NiSe nanoparticles on Ti plate achieved a low overpotential of 320 mV at 100 mA cm^{-2} towards the OER in 1.0 M KOH electrolyte.[6] The homogeneous Co-doped $MoSe_2$ shows excellent hydrogen evolution performance in

alkaline medium. Co-doping not only improves the hydrogen adsorption free energy, but also improves the water adsorption and dissociation ability.[25] Here, it is worth noting that a literature survey revealed that Co-doped nickel hydroxide as electrocatalyst has never been used for water splitting.

It is now well-accepted in the field that, for water electrolysis, the HER and OER are better suited to acidic and alkaline media respectively, as experimentally observed by the low HER and OER overpotentials.[28] The incompatibility of HER and OER for water electrolysis significantly affects the operating efficiency and thus results in high energy consumption. Therefore, developing HER and OER catalysts with similar synthetic procedures (to lower manufacturing costs and environmental waste) and compositions as asymmetric electrodes could avoid this problem, reduce the synthetic cost and simplify as well as lower the water electrolyser system´s cost (i.e. BoP – balance of plant).

Herein, Fe, Co doped nickel hydroxide nanosheets, directly formed onto the surface of Ni foam, were developed as non-PGM catalysts for the HER and OER. The Co-doped nickel hydroxide (denoted as Co-Ni$(OH)_2$) and Fe-doped nickel hydroxide (denoted as Fe-Ni$(OH)_2$) were synthesized via a similar synthetic procedure and used as HER and OER catalysts for water electrolysis respectively. In such an asymmetric water electrolyser, it was found that the water splitting cell could deliver a cell voltage of 1.59 V at a current density of 10 mA cm^{-2}, a value similar to that obtained water electrolysers containing Pt/C as HER and RuO_2 as OER catalysts.

2. Experimental methods

Binder-free M-doped $Ni(OH)_2$ (M = Fe or Co) ultra-thin nanosheet arrays were prepared by a facile one-pot method. The detailed synthesis process is as follows: before synthesizing $Ni(OH)_2$ onto Ni foam, the Ni foam with a size of 2 cm × 3 cm was immersed and ultrasonicated in a 1.0 M HCl solution for 10 minutes to remove any surface oxides. The treated Ni foam (NF) was washed with ultrapure water and ethanol sequentially, and then vacuum dried at 60°C. The dried NF was placed into 20 mL of 3.6 mM hydrochloric acid (HCl) solution containing *X* mmol of $Co(NO_3)_2 \cdot 6H_2O$ (*X* = 0.01, 0.03, 0.05 mmol), and then heated at 100°C for 20 h. The obtained NF was rinsed with ultrapure water and vacuum dried at 60°C. The dried sample was labelled as Co-$Ni(OH)_2$-*X* (*X* is the amount of $Co(NO_3)_2 \cdot 6H_2O$ used in the precursor). Other samples were also prepared by replacing the above $Co(NO_3)_2 \cdot 6H_2O$ with $Fe(NO_3)_3 \cdot 9H_2O$, and the rest of the above procedure remained the same. The obtained samples were denoted as Fe-$Ni(OH)_2$-*X* (*X* is the molar mass of $Fe(NO_3)_3 \cdot 9H_2O$ in 3.6 mM hydrochloric acid (HCl) solution). For comparison purposes, $Ni(OH)_2$ nanosheets grown on NF without introducing Co or Fe were prepared under similar experimental conditions. The product was denoted as $Ni(OH)_2$.

The physical characterization and electrochemical measurements are detailed in the *Supporting Information* section.

3. Results and discussion

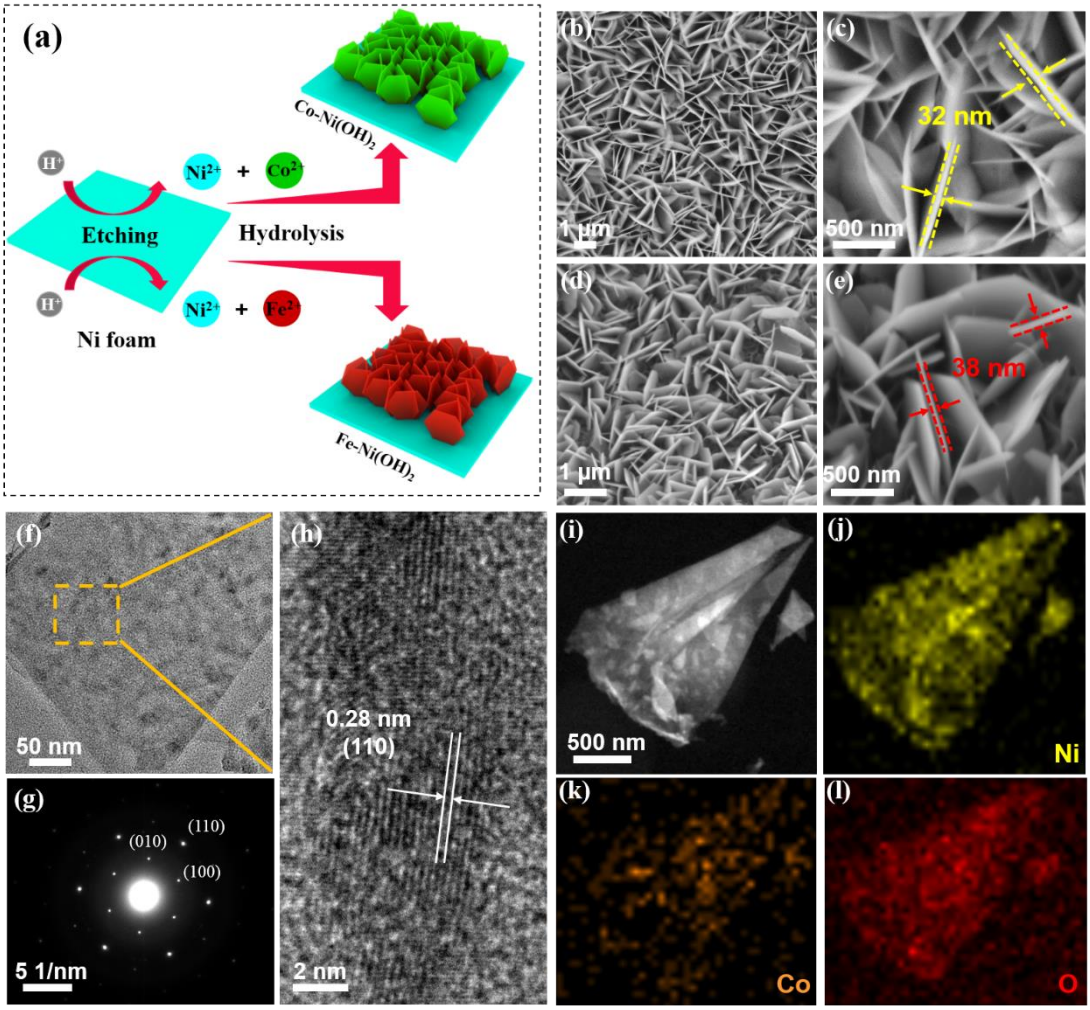

Figure1. (a) Schematic illustration of the synthesis of M-Ni(OH)$_2$; (b, c) SEM image of Co-Ni(OH)$_2$; (d, e) SEM image of Fe-Ni(OH)$_2$; (f) TEM; (g) SAED patterns and (h) HRTEM images of Co-Ni(OH)$_2$; (i-l) STEM and EELS elemental mappings of Ni, Co and O elements.

M-Ni(OH)$_2$ formed onto NF was performed via a facile one-pot method, in which the formation of Ni(OH)$_2$ nanosheets and M doping into Ni(OH)$_2$ occurred simultaneously. The formation of M-Ni(OH)$_2$ is schematically illustrated in Figure 1(a). In this method, the NF was used as nickel to form nickel hydroxide onto the surface of

NF via controlling the solution pH. We found that different concentrations of hydrochloric acid have a significant effect on the morphology of the nanoarrays(Figure S2). In the 3.6 mM HCl solution, the $Ni(OH)_2$ nanosheets are densely grown and the thickness is moderate. NF reacted with HCl to form Ni^{2+} via chemical etching. These new formed Ni^{2+} ions also reacted with OH^- in the same solution and formed $Ni(OH)_2$ onto the surface of NF. When Co^{2+} or Fe^{3+} ions were present in the same solution, these ions were able to penetrate into the crystal structure of $Ni(OH)_2$ during the formation of $Ni(OH)_2$ nanosheets. The obtained $Ni(OH)_2$, Co-$Ni(OH)_2$ and Fe-$Ni(OH)_2$ pictures are shown in Figure S1. Through this method, the formation of $Ni(OH)_2$ nanosheets and hetero-atom doping could occur simultaneously, which greatly simplified the synthetic procedure and thus could make them economically viable for large-scale applications.

SEM analyses were performed for revealing the morphology of the obtained M-$Ni(OH)_2$; their SEM images were displayed in Figure 1(b-e). It was observed that the pH and the concentration of the dopant solution had a critical impact on the morphology and structure of $Ni(OH)_2$ nanosheets. It was found that 3.6×10^{-3} M HCl was the optimised acid concentration for forming uniform and dense $Ni(OH)_2$ nanosheets onto NF. As shown in Figure 1(b) and 1(d), three-dimensional (3-*D*) and interconnected nanosheets were evenly formed onto the surface of NF. The thickness of these nanosheets were found to be ca. 32-38 nm (Figure 1(c) and 1(e)). These SEM images also clearly demonstrate that introducing moderate Co or Fe salts into the precursor does not have any obvious impacts on the obtained morphology. It was also observed that uniform and interconnected nanosheets were obtained as indicated from the SEM

images of both Co-Ni$(OH)_2$ and Fe-Ni$(OH)_2$. Compared to Co-Ni$(OH)_2$, the average sizes and thicknesses of Fe-Ni$(OH)_2$ nanosheets were slightly larger than those found for Co-Ni$(OH)_2$. Moreover, the quantities of $Co(NO_3)_2$ and $Fe(NO_3)_3$ in the precursor affected the morphology of Co-Ni$(OH)_2$ and Fe-Ni$(OH)_2$. For quantities of $Co(NO_3)_2$ and $Fe(NO_3)_3$ lower than 0.01 mmol, the produced interconnected nanosheets of rough surfaces were observed as shown in Figure S3(a) and S3(b). For Fe-Ni$(OH)_2$-0.01, winding nanosheets containing rough surfaces were formed onto NF. When the amount of $Co(NO_3)_2$ and $Fe(NO_3)_3$ was 0.03 mmol, straight nanosheets of smooth surfaces were obtained (Figure 2(b) and 2(d)). However, the nanosheet structure disappeared and irregular particles were formed when the amount of $Co(NO_3)_2$ and $Fe(NO_3)_3$ further increased to 0.05 mmol. This finding indicates that the amount of $Co(NO_3)_2$ and $Fe(NO_3)_3$ makes a great effect on the morphology of the obtained Co-Ni$(OH)_2$ and Fe-Ni$(OH)_2$ materials.

The detailed structures of Co-Ni$(OH)_2$ and Fe-Ni$(OH)_2$ (X = 0.03 mmol) were also evaluated by transmission electron microscopy (TEM). Figure 1(f) shows that the surface of the nanosheets was filled with many nano-sized dark dots. Well-defined lattice fringes are clearly shown in the high-resolution TEM image (Figure 1(h)), indicating its crystal structure. The interplanar distance was found to be ca. 0.28 nm, which corresponded to the (110) plane of $Ni(OH)_2$. The TEM image of Fe-Ni$(OH)_2$ (Figure S4(a)) is similar-*ish* to that of Co-Ni$(OH)_2$. Well-defined lattice fringes with an interplanar distance of ca. 0.28 nm can be ascribed to the (110) plane of $Ni(OH)_2$ as shown in Figure S4(b). The SAEM patterns of Co-Ni$(OH)_2$ exhibited a set of well-

defined dots due to its high crystallinity and monocrystal structure (Figure 1(g)). SAEM patterns of Fe-Ni(OH)$_2$ (Figure S4(c)) also indicated high crystal and monocrystal features. The elemental mappings of Ni, Co and O elements were investigated by HAADF-STEM (Figure 1(i-l)), showing that Ni, Co and O elements were evenly distributed onto the selected particle, and the amount of Co element was obviously lower than that of the other two elements. For Fe-Ni(OH)$_2$, the STEM and EELS elemental mapping demonstrated that the Ni, Fe and O elements were uniformly dispersed (Figure S4(d-g)).

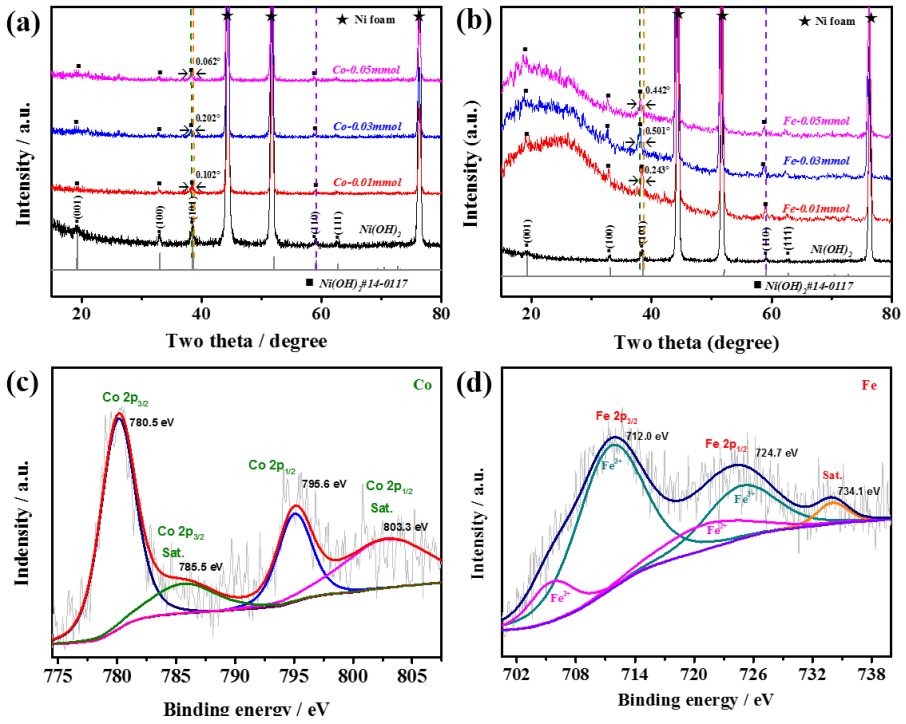

Figure 2. XRD patterns of the Co-Ni(OH)$_2$ and Fe-Ni(OH)$_2$ (a,b); the deconvoluted high-resolution XPS spectra of Co 2*p* (c) and Fe 2*p* (d).

X-ray diffraction (XRD) analysis was further carried out to evaluate the crystal structures of Co-Ni(OH)$_2$ and Fe-Ni(OH)$_2$ (Figure 2(a) and 2(b)). Apart from the major diffraction peaks of Ni foam at 44.2, 51.6 and 76.2°, the characteristic diffraction peaks

of $Ni(OH)_2$ (Joint Committee on Powder Diffraction Standards Card (JCPDS) No.14-0117) are clearly shown in the XRD pattern of Co-$Ni(OH)_2$ (Figure 2(a)). It was found that, by increasing the amount of $Co(NO_3)_2$ in the precursor, the diffraction peaks continuously shifted to the low angle region since more and more Co ions penetrated into the crystal structure of $Ni(OH)_2$. Except for the NF and $Ni(OH)_2$ diffraction peaks, no other peaks related to cobalt oxides and hydroxides were found in the XRD pattern, suggesting that Co ions were present in the structure of $Ni(OH)_2$. In the XRD pattern of Fe-$Ni(OH)_2$ (Figure 2(b)), it can be observed that the diffraction peaks also shifted to the low angle region due to the presence of $Fe(OH)_3$, suggesting that Fe ions were intercalated into the $Ni(OH)_2$. Moreover, it was observed that no crystal forms of Fe species were detected in the Fe-$Ni(OH)_2$ samples. These XRD results indicated that Co and Fe doped $Ni(OH)_2$ were formed by this simple one-pot synthetic method.

The chemical state and composition on the surface of Co-$Ni(OH)_2$ and Fe-$Ni(OH)_2$ were analysed by X-ray photoelectron spectroscopy (XPS). The Ni, Co, Fe and O elements were detected in their corresponding survey spectra of Co-$Ni(OH)_2$ and Fe-$Ni(OH)_2$ (Figure S5(a) and S5(d)). The Co and Fe atom content in the surface was 11.67% and 10.66% of the Co-$Ni(OH)_2$ and Fe-$Ni(OH)_2$ catalysts respectively. The high-resolution Ni 2*p* XPS spectra of Co-$Ni(OH)_2$ and Fe-$Ni(OH)_2$ (Figure S5(b) and S5(e)) can be deconvoluted into two doublet accompanied with two satellite peaks, which can be ascribed to the Ni^{2+} in $Ni(OH)_2$[29]. The peaks at 529.1 eV, 530.2 eV and 530.9 eV attributed to O^{2-}, OH and H_2O_{ab} respectively [30] were observed in the high-resolution O 1*s* spectra of Co-$Ni(OH)_2$ and Fe-$Ni(OH)_2$ (Figure S5(c) and S5(f)). The XPS spectra

confirmed that $Ni(OH)_2$ was formed in both Co-$Ni(OH)_2$ and Fe-$Ni(OH)_2$ samples. The Co 2*p* XPS spectrum of Co-$Ni(OH)_2$ shows two peaks corresponding to Co $2p_{3/2}$ and Co $2p_{1/2}$ at 780.5 and 795.6 eV respectively (Figure 2(c)), However, the extremely low intensity of the two satellites (at ca. 785.5 and 803.4 eV) is attributed to the partial oxidation of the Co^{2+} ions, which stimulates charge transfer in the electrochemical process.[6, 31] For Fe-$Ni(OH)_2$, Two sets of typical 2p peaks of Fe^{3+} (712.0 and 724.7 eV) and Fe^{2+} (706.9 and 722.3 eV) ions of the Fe–$Ni(OH)_2$ sample further verify the successful incorporation and partial reduction of Fe^{3+} ions. (Figure 2(d)).[17, 32]

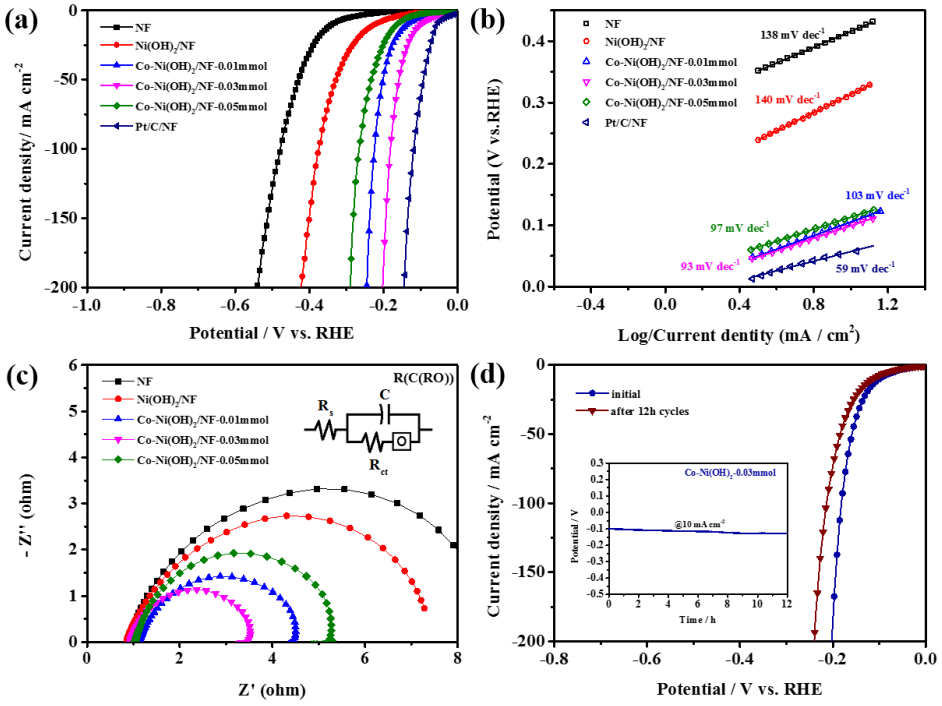

Figure 3. (a) HER LSVs of Co-$Ni(OH)_2$-*X* samples, $Ni(OH)_2$/NF, Pt/C/NF electrodes in 1.0 M KOH at a scan rate of 5 mV s^{-1}; (b) their Tafel plots; (c) Nyquist plots at -0.17 V *vs. RHE*; (d) HER LSVs of the Initial and the one after 12 hour cycle on Co-$Ni(OH)_2$/NF-0.03 mmol in 1.0 M KOH at a scan rate of 5 mV s^{-1} (Inset: long-term chronopotentiometry of Co-$Ni(OH)_2$/NF-0.03 at 10 mA cm^{-2} for 12 h).

The HER behaviour of Co-Ni$(OH)_2$-0.03 was determined by linear sweep voltammetry (LSV), carried out in 1.0 M KOH electrolyte at a scan rate of 5 mV s^{-1} (Figure 3(a)). Figure 3(a) shows that Pt/C/NF exhibited the highest activity towards the HER. Compared to NF and $Ni(OH)_2$, the LSV curves of Co-Ni$(OH)_2$-*X* samples presented much lower onset potentials and lower overpotentials at the employed current density range, indicating that doping Co ions into the structure of $Ni(OH)_2$ can significantly improve the HER activity. The overpotential at 10 mA cm^{-2} was also compared with many representative TMB HER catalysts (Figure S6(b) and Table S3), showing that the Co-Ni$(OH)_2$-0.03 is one of the best in class. The HER mechanism on Co-Ni$(OH)_2$-X was investigated by the Tafel slope method (Figure 3(b)). The Tafel slopes of Co-Ni$(OH)_2$-0.01, Co-Ni$(OH)_2$-0.03 and Co-Ni$(OH)_2$-0.05 were 103, 93 and 97 mV dec^{-1} respectively; values which were much lower than the Tafel slope values of NF and $Ni(OH)_2$/NF, demonstrating that moderate Co doping could efficiently improve the HER kinetics and thus the hydrogen generation rate. The result could be ascribed to the fact that Co-Ni$(OH)_2$-0.03 has a more dense nanosheet array with a moderate thickness, which display many advantages, including large exposer , more active sites, thus facilitating the electrochemical process between the ionic and electron transport of active materials and substrates.[33] Here, the HER could be divided into three possible steps, namely the Tafel reaction ($H_{ad} + H_{ad} \rightarrow H_2$), the Heyrovsky reaction ($H_3O^+ + e^{-1} + H_{ad} \rightarrow H_2 + H_2O$) and the Volmer reaction ($H_3O^+ + e^{-1} \rightarrow H_{ad} + H_2O$).[34] Based upon the Tafel slope values, it can be stated that the HER occurring onto the Co-Ni$(OH)_2$-*X* samples involved the Volmer-Heyrovsky steps, where the

electrochemical desorption is the rate-determining step (*rds*). The charge transfer resistance of HER on Co-Ni$(OH)_2$-*X* samples was further studied by generating Nyquist plots via electrochemical impedance spectroscopy (EIS). Usually in EIS, lower Nyquist plot radii represent lower charge transfer resistance. As shown in Figure 3(c), the Nyquist plot for Co-Ni$(OH)_2$-0.03 has the smallest radius among all the tested samples, and the fitting values for the electrochemical components in Nyquist plots in Table S1 indicate that Co-Ni$(OH)_2$-0.03 has a low charge transfer resistance. The durability of Co-Ni$(OH)_2$-*X* samples towards the HER were measured by continuous linear sweep voltammetry (LSV) cycling and by chronopotentionmetry at 10 mA cm^{-2} (Figure 3(d)). The electrochemical surface areas (ECSA) of these electrodes were evaluated by their corresponding electrochemical double-layer capacitances (EDLC), which were measured by cyclic voltammetry (Figure S7). The capacitance of Co-Ni$(OH)_2$-0.03 was found to be 1.2 mF cm^{-2}, a value much higher than that of Co-Ni$(OH)_2$-0.01, Co-Ni$(OH)_2$-0.05 and Ni$(OH)_2$. This finding suggests that more electrocatalytic active sites are available on the surface of Co-Ni$(OH)_2$-0.03. The overpotential at 50 mA cm^{-2} shifted ca. 30 mV negatively after 12 hours of continuous LSV, indicating that Co-Ni$(OH)_2$-0.03 is more stable than the state-of-the-art HER catalyst, Pt/C (Figure S8).

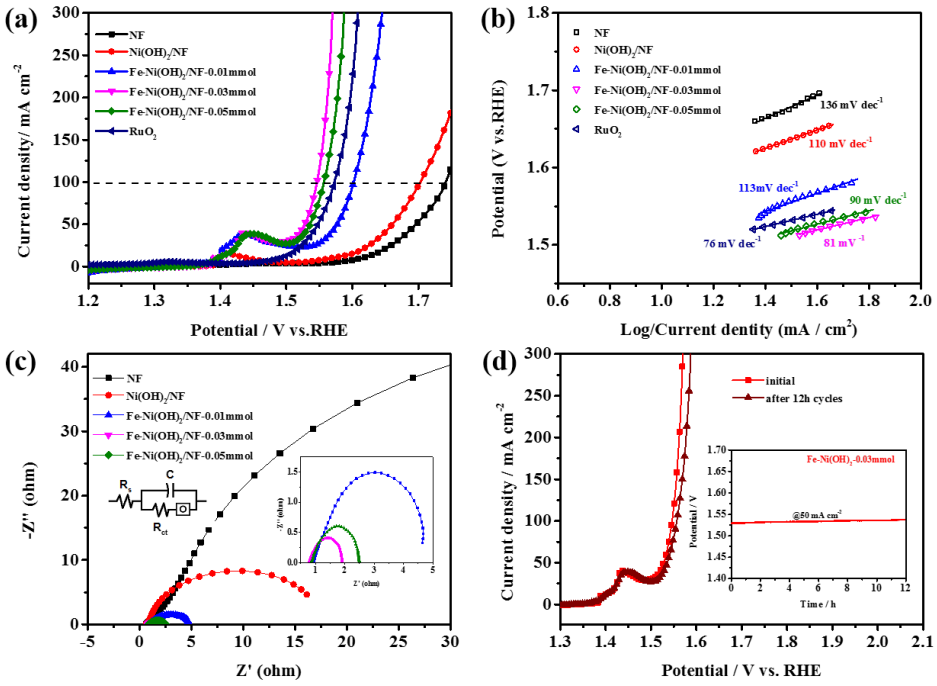

Figure 4. (a) OER LSVs of Fe-Ni(OH)$_2$-*X* (*X* = 0.01, 0.03 and 0.05 mmol) samples, Ni(OH)$_2$, RuO$_2$/NF electrodes in 1.0 M KOH at a scan rate of 5 mV s^{-1}; (b) their Tafel plots; (c) Nyquist plots at +1.52 V *vs. RHE*; (d) HER LSVs of the initial curve and the one after 12 h cycle on Fe-Ni(OH)$_2$-0.03 in 1.0 M KOH at a scan rate of 5 mV s^{-1} (Inset: long-term chronopotentiometry of Fe-Ni(OH)$_2$-0.03 at 10 mA cm^{-2} for 12 hours)

The electrocatalytic activity towards the OER was also evaluated by LSV in 1.0 M KOH electrolyte (Figure 4(a) and Figure S5(a)). From the figures, it is evident that the OER activity of Fe doped Ni(OH)$_2$ sample greatly surpasses of the Ni(OH)$_2$ and NF samples, suggesting that the OER activity can be enhanced by doping Fe ions into Ni(OH)$_2$. The OER activity of Fe-Ni(OH)$_2$-0.03 and Fe-Ni(OH)$_2$-0.05 samples were even higher than that of RuO$_2$. At a current density of 50 mA cm^{-2}, the OER overpotential for Fe-Ni(OH)$_2$ was also compared with the values reported in the literature (Figure S6(c) and Table S4). The OER kinetics of these electrodes were

further investigated by the Tafel plot method (Figure 5(c)). The Tafel slopes of Fe-$Ni(OH)_2$-0.03, RuO_2/NF, $Ni(OH)_2$/NF and NF were found to be 81, 76, 110 and 136 mV dec^{-1} respectively. The Fe-$Ni(OH)_2$-0.03 exhibited the lowest Tafel slope value among all the samples. The OER charge resistance on these materials was further studied by EIS analysis. In the high frequency region, the semi-circles of their Nyquist plots show that Fe-$Ni(OH)_2$-0.03 had the lowest charge transfer resistance during the OER process(Table S2). The durability of these *as*-prepared samples towards the OER were also performed by both continuous OER LSV cycling and chronopotentionmetry at 50 mA cm^{-2}. After 12 hours of continuous OER LSV cycling, the overpotential at 100 mA cm^{-2} only increased by 10 mV. As shown in the long-term chronopotentiometry measurement for Fe-$Ni(OH)_2$-0.03, no obvious decay in overpotential was observed, further indicating its excellent durability towards the OER.

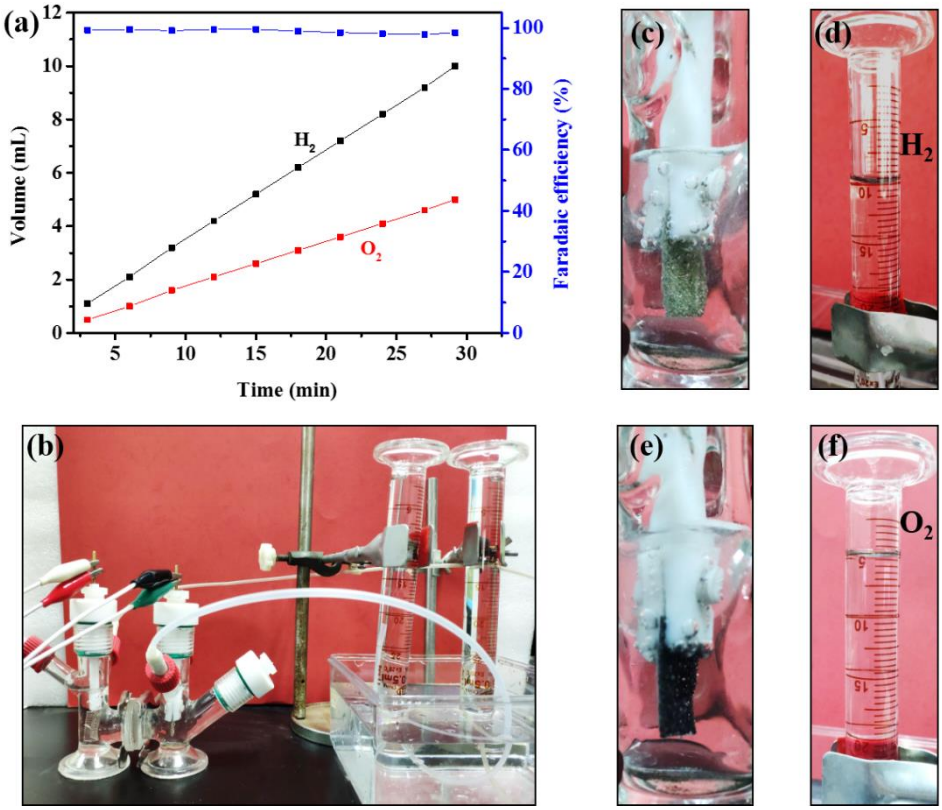

Figures 5. Gas volume *versus* time and corresponding faradaic efficiency (a); two-electrode configuration for water splitting (b); gases generated on the anode and cathode respectively (c,e); (d,f) collected H_2 and O_2.

The electrochemical performance of Co-Ni$(OH)_2$-0.03 and Fe-Ni$(OH)_2$-0.03 as HER and OER catalysts respectively was evaluated in "real world" water splitting conditions, in which two graduated cylinders were used to collect the generated oxygen (anode) and hydrogen (cathode) (Figure 5). It was found that the water splitting (1.0 M KOH) occurred on these electrodes at an impressive cell voltage of 1.59 V. In our conditions, the current density reached 50 mA cm^{-2} when the cell voltage was ca. 1.70 V, and the generated oxygen and hydrogen gases were constantly kept at stoichiometric ratio of 1:2 as shown in Figures 5(d) and 5(f). The assembled water splitting cell using the cathode and anode with a size of 1 cm ×1 cm generated 10 ml H_2 within 29 min of electrolysis, together with a faradaic efficiency closed to 100 %.

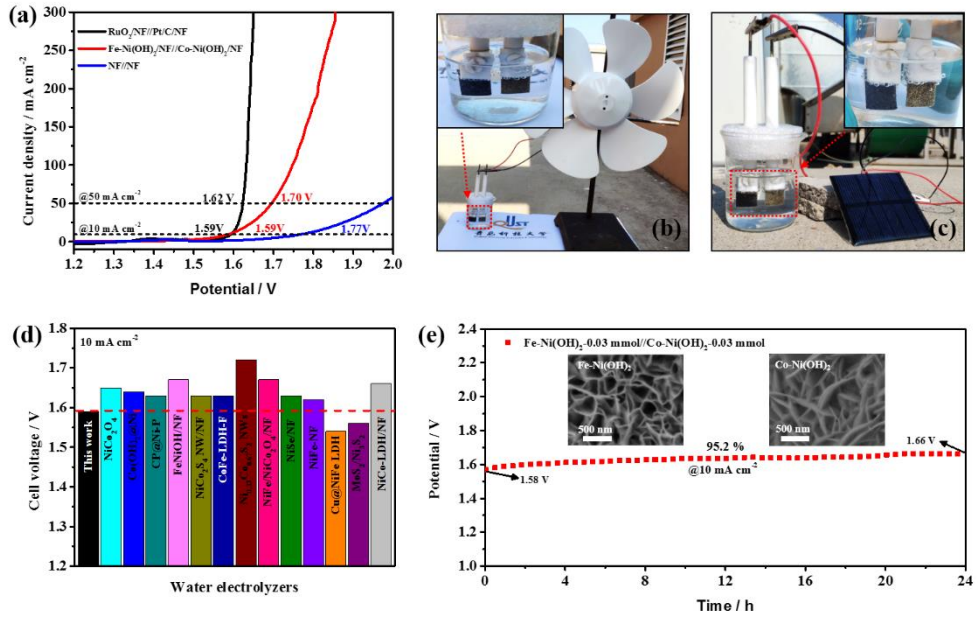

Figure 6. (a) LSV curves obtained for water electrolysis on Fe-Ni$(OH)_2$//Co-Ni$(OH)_2$,

NF//NF, and RuO_2/NF//Pt/C/NF immersed in 1.0 M KOH electrolyte, in a two-electrode configuration at a scan rate of 5 mV s^{-1}; (b,c) Using wind and solar energy as renewable energy to drive the in-house built water electrolyser, respectively； (d) Comparison of cell voltages of different dual-function electrodes to achieve 10 mA cm^{-2} among various water alkaline electrolyser catalysts；(e) chronopotentiometry curve obtained for water electrolysis on Fe-$Ni(OH)_2$//Co-$Ni(OH)_2$ in a two-electrode configuration and at a constant current density of 10 mA cm^{-2}.

As shown in Figure 6(a), the electrodes made of Fe-$Ni(OH)_2$//Co-$Ni(OH)_2$, NF//NF, and RuO_2/NF//Pt/C/NF immersed in 1.0 M KOH, could deliver a current density of 10 mA cm^{-2} at a cell voltage of 1.59, 1.77 and 1.59 V respectively, further confirming that the Fe-$Ni(OH)_2$ and Co-$Ni(OH)_2$ are highly electrocatalytically active towards the OER and HER respectively in an asymmetric water splitting cell. When the current density was further increased to 50 mA cm^{-2}, the cell voltages for the electrodes made of Fe-$Ni(OH)_2$//Co-$Ni(OH)_2$, NF//NF, and RuO_2/NF//Pt/C/NF were 1.70, 1.98 and 1.62 V respectively. Although the cell voltage of Fe-$Ni(OH)_2$//Co-$Ni(OH)_2$ at 50 mA cm^{-2} is lower than that of RuO_2/NF//Pt/C/NF, it is higher than most of the transitional metal based bifunctional water electrolysers reported in the literature (Figure 6(d) and Table S5).

The Fe-$Ni(OH)_2$//Co-$Ni(OH)_2$ electrodes immersed in 1.0 M KOH were connected to a portable wind turbine and a solar panel as external power sources. As shown in Figure 6, plenty of bubbles were generated on the surface of both electrodes when the

portable renewable energy systems (RES) were working, demonstrating the great potential of both the *a*s-prepared electrodes for use in water splitting to produce hydrogen from RES. The Fe-$Ni(OH)_2$//Co-$Ni(OH)_2$ water splitting cell also exhibited a good stability for water splitting, whereby an operating cell voltage only increased by 80 mV after the cell operated at a current density of 10 mA cm^{-2} for 24 hours (Figure 6(e)). After this 24 h testing, the morphology of Fe-$Ni(OH)_2$ and Co-$Ni(OH)_2$ was further analysed by SEM, and no changes were noticeable. The above findings demonstrate that the *a*s-prepared Co-$Ni(OH)_2$ and Fe-$Ni(OH)_2$ have highly electrocatalytic activity towards the HER and OER respectively. Due to the facile one-pot synthetic procedure, these bind-free electrodes for the HER and OER are promising electrocatalysts for water splitting.

4. Conclusions

Fe and Co doped nickel hydroxides can be easily and directly produced onto the surface of Ni foam via controlling the pH value without using any nickel salt as precursor. Using this method, the formation of nano-sized nickel hydroxide and hetero-atom doping could occur simultaneously, which significantly simplifies the synthetic procedure. The SEM results showed that three-dimensional and interconnected nanosheets were evenly formed onto the surface of the nickel foam. HER experiments showed that doping Co ions into the structure of $Ni(OH)_2$ could significantly improve the HER activity. The OER activity of the Fe doped $Ni(OH)_2$ revealed that OER activity could also be enhanced by doping Fe ions into $Ni(OH)_2$. When Fe-$Ni(OH)_2$ and Co-$Ni(OH)_2$ were used as HER and OER in a two-electrode water electrolyser set-up, the

Fe-Ni(OH)$_2$//Co-Ni(OH)$_2$ water splitting cell delivered a current density of 10 mA cm^{-2} at a cell voltage of 1.59 V. The cell voltage of the Fe-Ni(OH)$_2$//Co-Ni(OH)$_2$ electrodes immersed in 1.0 M KOH at 10 mA cm^{-2} was the same than that of a cell made RuO_2/NF//Pt/C/NF electrodes. Since the Fe-Ni(OH)$_2$ and Co-Ni(OH)$_2$ can be produced via a facile one-pot method without using any additional nickel salt as precursor, these Fe-Ni(OH)$_2$ and Co-Ni(OH)$_2$ are thought to be promising HER and OER catalysts for highly-efficient water splitting applications.

Acknowledgment

The authors would like to thank the National Natural Science Foundation of China (51661008 and 21766032) and Key Research and Development Program of Shandong Province of China (2019GGX103029) for financially supporting this work.

References：

[1] J. Ding, P. Wang, S. Ji, H. Wang, D.J.L. Brett, R. Wang, Mesoporous nickel selenide N-doped carbon as a robust electrocatalyst for overall water splitting, Electrochimi. Acta, 300 (2019) 93-101.

[2] R. Wang, Y. Ma, H. Wang, J. Key, S. Ji, Gas–liquid interface-mediated room-temperature synthesis of “clean” PdNiP alloy nanoparticle networks with high catalytic activity for ethanol oxidation, Chem. communications, 50 (2014) 12877-12879.

[3] Z. Wang, H. Wang, S. Ji, X. Wang, B.G. Pollet, R. Wang, Multidimensional regulation of Ni_3S_2@Co(OH)$_2$ catalyst with high performance for wind energy electrolytic water, J. Power Sources, 446 (2020) 227348.

[4] J. Wang, X. Ma, F. Qu, A.M. Asiri, X. Sun, Fe-Doped Ni_2P Nanosheet Array for High-Efficiency Electrochemical Water Oxidation, Inorg. Chem. 56 (2017) 1041-1044.

[5] Y. Rao, Y. Wang, H. Ning, P. Li, M. Wu, Hydrotalcite-like Ni(OH)$_2$ Nanosheets in Situ Grown on Nickel Foam for Overall Water Splitting, ACS Appl. Mater. Interfaces 8 (2016) 33601-33607.

[6] T. Liu, A.M. Asiri, X. Sun, Electrodeposited Co-doped $NiSe_2$ nanoparticles film: a good electrocatalyst for efficient water splitting, Nanoscale, 8 (2016) 3911-3915.

[7] J. Ding, S. Ji, H. Wang, B.G. Pollet, R. Wang, Mesoporous CoS/ N-doped Carbon as HER and ORR Bifunctional Electrocatalyst for Water Electrolysers and Zinc-Air Batteries, ChemCatChem, 0 (2019).1026-1032.

[8] Y. Yan, B. Xia, B. Zhao, X. Wang, A review on noble-metal-free bifunctional heterogeneous catalysts for overall electrochemical water splitting, J. Mater. Chem. A. 4 (2016) 17587-17603.

[9] X. Wang, W. Li, D. Xiong, D.Y. Petrovykh, L. Liu, Bifunctional Nickel Phosphide Nanocatalysts Supported on Carbon Fiber Paper for Highly Efficient and Stable Overall Water Splitting, Adv. Funct. Mater. 26 (2016) 4067-4077.

[10] J. Ding, S. Ji, H. Wang, V. Linkov, H. Gai, F. Liu, Q. Liu, R. Wang, N-Doped 3D Porous Ni/C Bifunctional Electrocatalysts for Alkaline Water Electrolysis, ACS Sus. Chem. Eng. 7 (2019) 3974-3981.

[11] Z. Wang, S. Ji, F. Liu, H. Wang, X. Wang, Q. Wang, B.G. Pollet, R. Wang, Highly Efficient and Stable Catalyst Based on $Co(OH)_2$@Ni Electroplated on Cu-Metallized Cotton Textile for Water Splitting, ACS Appl. Mater. Interfaces, 11 (2019) 29791-29798.

[12] K. Fominykh, P. Chernev, I. Zaharieva, J. Sicklinger, G. Stefanic, M. Döblinger, A. Müller, A. Pokharel, S. Böcklein, C. Scheu, T. Bein, D. Fattakhova-Rohlfing, Iron-Doped Nickel Oxide Nanocrystals as Highly Efficient Electrocatalysts for Alkaline Water Splitting, ACS Nano, 9 (2015) 5180-5188.

[13] Q. Zhou, Z. Shen, C. Zhu, J. Li, Z. Ding, P. Wang, F. Pan, Z. Zhang, H. Ma, S. Wang, H. Zhang, Nitrogen-Doped CoP Electrocatalysts for Coupled Hydrogen Evolution and Sulfur Generation with Low Energy Consumption, Adv. Mater. 30 (2018) 1800140.

[14] M. Xiao, Y. Miao, Y. Tian, Y. Yan, Synthesizing Nanoparticles of Co-P-Se compounds as Electrocatalysts for the Hydrogen Evolution Reaction, Electrochim. Acta, 165 (2015) 206-210.

[15] X. Gao, H. Zhang, Q. Li, X. Yu, Z. Hong, X. Zhang, C. Liang, Z. Lin, Hierarchical $NiCo_2O_4$ Hollow Microcuboids as Bifunctional Electrocatalysts for Overall Water-Splitting, Angew Chem. Int. Edit. 55 (2016) 6290-6294.

[16] P.F. Liu, S. Yang, B. Zhang, H.G. Yang, Defect-Rich Ultrathin Cobalt-Iron Layered Double Hydroxide for Electrochemical Overall Water Splitting, ACS Appl. Mater. Interfaces, 8 (2016) 34474-34481.

[17] J.T. Ren, G.G. Yuan, C.C. Weng, L. Chen, Z.Y. Yuan, Uniquely integrated Fe-doped $Ni(OH)_2$ nanosheets for highly efficient oxygen and hydrogen evolution reactions, Nanoscale, 10 (2018) 10620-10628.

[18] Q. Xu, H. Jiang, H. Zhang, Y. Hu, C. Li, Heterogeneous interface engineered atomic configuration on ultrathin $Ni(OH)_2/Ni_3S_2$ nanoforests for efficient water splitting, Appl. Catal. B-Environ. 242 (2019) 60-66.

[19] N. Hussain, W. Yang, J. Dou, Y. Chen, Y. Qian, L. Xu, Ultrathin mesoporous F-doped α-$Ni(OH)_2$ nanosheets as an efficient electrode material for water splitting and supercapacitors, J. Mater. Chem. A. 7 (2019) 9656-9664.

[20] N. Danilovic, R. Subbaraman, D. Strmcnik, K.C. Chang, A.P. Paulikas, V.R. Stamenkovic, N.M. Markovic, Enhancing the alkaline hydrogen evolution reaction activity through the bifunctionality of $Ni(OH)_2$/metal catalysts, Angew Chem. Int. Edit. 51 (2012) 12495-12498.

[21] N. Mahmood, Y. Yao, J.W. Zhang, L. Pan, X. Zhang, J.J. Zou, Electrocatalysts for Hydrogen Evolution in Alkaline Electrolytes: Mechanisms, Challenges, and Prospective Solutions, Adv. Sci. 5 (2018) 1700464.

[22] H. Wu, X. Lu, G. Zheng, G.W. Ho, Topotactic Engineering of Ultrathin 2D Nonlayered Nickel Selenides for Full Water Electrolysis, Adv. Energy Mater. 8 (2018).1702704.

[23] X. Du, Z. Yang, Y. Li, Y. Gong, M. Zhao, Controlled synthesis of $Ni(OH)_2/Ni_3S_2$ hybrid nanosheet arrays as highly active and stable electrocatalysts for water splitting, J. Mater. Chem. A. 6 (2018) 6938-6946.

[24] G. Zhao, P. Li, K. Rui, Y. Chen, S.X. Dou, W. Sun, $CoSe_2$ /$MoSe_2$ Heterostructures with Enriched Water Adsorption/Dissociation Sites towards Enhanced Alkaline Hydrogen Evolution Reaction, Chem-Eur. J. 24 (2018) 11158-11165.

[25] O. Zimron, T. Zilberman, S.R. Kadam, S. Ghosh, S.L. Kolatker, A. Neyman, R. Bar-Ziv, M. Bar-Sadan, Co-doped $MoSe_2$ Nanoflowers as Efficient Catalysts for Electrochemical Hydrogen Evolution Reaction (HER) in Acidic and Alkaline Media, Isr. J. Chem. 60 (2020) 1-7.

[26] S. Klaus, M.W. Louie, L. Trotochaud, A.T. Bell, Role of Catalyst Preparation on the Electrocatalytic Activity of $Ni_{1-x}Fe_xOOH$ for the Oxygen Evolution Reaction, J. Phys. Chem. C, 119 (2015) 18303-18316.

[27] D. Friebel, M.W. Louie, M. Bajdich, K.E. Sanwald, Y. Cai, A.M. Wise, M.-J. Cheng, D. Sokaras, T.-C. Weng, R. Alonso-Mori, R.C. Davis, J.R. Bargar, J.K. Nørskov, A. Nilsson, A.T. Bell, Identification of Highly Active Fe Sites in (Ni,Fe)OOH for Electrocatalytic Water Splitting, J. Am. Chem. Soc. 137 (2015) 1305-1313.

[28] E.A. Hernández-Pagán, N.M. Vargas-Barbosa, T. Wang, Y. Zhao, E.S. Smotkin, T.E. Mallouk, Resistance and polarization losses in aqueous buffer–membrane electrolytes for water-splitting photoelectrochemical cells, Energ. Environ. Sci. 5 (2012) 7582-7589.

[29] F. Chen, H. Wang, S. Ji, V. Linkov, R. Wang, Core-shell structured Ni_3S_2@$Co(OH)_2$ nano-wires grown on Ni foam as binder-free electrode for asymmetric supercapacitors, Chem. Eng. J. 345 (2018) 48-57.

[30] H. Wu, X. Lu, G. Zheng, G.W. Ho, Topotactic Engineering of Ultrathin 2D Nonlayered Nickel Selenides for Full Water Electrolysis, Adv. Energy Mater. 8 (2018) 1702704.

[31] L. Ye, L. Zhao, H. Zhang, P. Zan, S. Gen, W. Shi, B. Han, H. Sun, X. Yang, T. Xu, Serpent-cactus-like Co-doped $Ni(OH)_2$/Ni_3S_2 hierarchical structure composed of ultrathin nanosheets for use in efficient asymmetric supercapacitors, J. Mater. Chem. A. 5 (2017) 1603-1613.

[32] H. Wu, T. Zhu, X. Lu, G.W. Ho, High-efficient electrocatalysts by unconventional acid-etching for overall water splitting, J. Mater. Chem. A. 5 (2017) 24153-24158.

[33] W. Xi, G. Yan, H. Tan, L. Xiao, S. Cheng, S.U. Khan, Y. Wang, Y. Li, Superaerophobic P-doped $Ni(OH)_2$/$NiMoO_4$ hierarchical nanosheet arrays grown on Ni foam for electrocatalytic overall water splitting, Dalton Trans. 47 (2018) 8787-8793.

[34] M. Wang, R. Ding, X. Cui, L. Qin, J. Wang, G. Wu, L. Wang, B. Lv, CoP porous hexagonal nanoplates in situ grown on RGO as active and durable electrocatalyst for hydrogen evolution, Electrochim. Acta, 284 (2018) 534-541.

Credit Author Statement

Yutai Wu：Methodology，Validation，Writing - Original Draft

Shan Ji：Conceptualization Resources，Writing - Review & Editing

Hui Wang: Validation, Writing - Original Draft

Bruno G. Pollet: Writing - Review & Editing

Xuyun Wang：Visualization

Rongfang Wang：Conceptualization Resources，Supervision